Supporting Information for:

Size Dependent Deformation of Nanocrystalline Pt Nanopillars

X. Wendy Gu[†], *Colleen N. Loynachan*[□], *Zhaoxuan Wu*[°], *Yong-Wei Zhang*[°], *David J. Srolovitz*[°+], *Julia R. Greer*[‡]*

[†]Division of Chemistry and Chemical Engineering, and [‡]Division of Engineering and Applied Science, California Institute of Technology, 1200 E. California Blvd., Pasadena, CA 91125, United States

[□]Department of Materials Science and Engineering, Massachusetts Institute of Technology, 77 Massachusetts Avenue, Cambridge, MA 02139, United States

[°]Institute of High Performance Computing, 1 Fusionopolis Way, #16-16 Connexis, Singapore 138632

[+]Departments of Materials Science and Engineering & Mechanical Engineering and Applied Mechanics, University of Pennsylvania, Philadelphia, PA 19104, United States

Measurement artifacts due to geometric imperfections at pillar top surface

One major benefit of micro- and nanopillar compression testing is that the pillar sample geometry lends itself to easy analysis and allows intrinsic material properties to be decoupled from geometric effects such as strain-gradients[1,2]. Geometric imperfections such as taper of the pillar walls and misalignment between pillar and tip must be minimized to create a uniaxial

stress state[3]. This work revealed that the morphology of the cylinder top, which makes the initial contact with the indenter tip upon compression, should also be carefully controlled.

We analyzed the stress-strain signatures of pillars whose top surface roughness was systematically varied. Between 5 and 14 measurements were made for each of the data points discussed here. Linear regression was performed on the loading and unloading portions of the stress-strain curves to find the loading and unloading moduli. Pillars with unloading moduli less than 65 GPa were not included because such a low unloading modulus was most likely due to poor alignment between pillar and tip, which resulted in pillar bending rather than compression.

We used focused ion beam (FIB) to smooth the top surface of the pillar. Figure S1a shows an as-electroplated nanopillar with a diameter of approximately 1 μm. The top surface of the nanopillar shows typical fractal-like surface roughness. Figure S1b shows a 1 μm sized nanopillar with the top surface gently polished with a low current FIB beam directed perpendicular to the pillar z-axis. The surface of this pillar is much smoother than the pillar in figure S1a (a quantitative determination of surface roughness is difficult to obtain from SEM images or via any other technique that we have attempted). Figure S1c shows a set of characteristic stress-strain curves for two representative as-electroplated (rough top) and polished (flat top) 1 μm-diameter pillars. The slope of the elastic loading portion in the stress-strain curve (loading modulus) was 60% lower for the pillars with rough surfaces. Compressing the as-fabricated samples, therefore, would lead to a 20% underestimation in the plastic flow stresses.

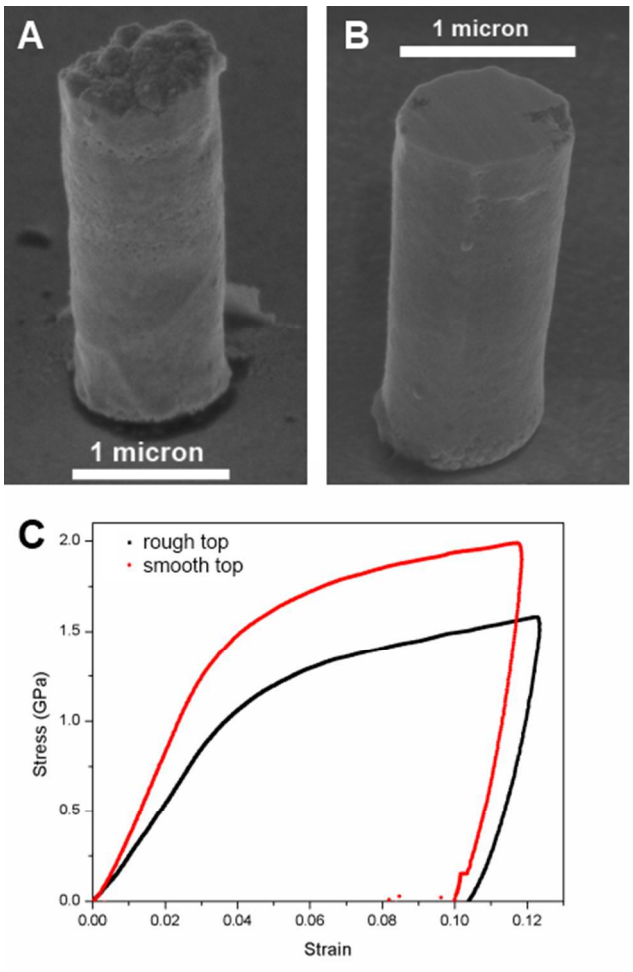

Figure S1. Effect of surface roughness on mechanical behavior of 1 µm sized pillars. SEM images of A) a typical as-electroplated pillar (rough top) and B) a pillar whose top surface was polished with FIB (smooth top). C) Typical stress-strain data for 1 µm sized samples with rough and smooth tops.

The influence of surface roughness can also be seen in pillars that are approximately 100 nm in diameter, albeit to a smaller degree. Figure S2a shows an as-electroplated 100 nm wide nanopillar, which had a naturally smooth and flat pillar top from the growth process. Applying a similar FIB-based methodology to these much smaller samples resulted in the hemispherical rather than flat top shapes because of the preferential milling at the edge of the cylinder (thinner area) compared to the center of the cylinder (thicker area) (figure S2b). The stress-strain curves

for 100 nm pillar compressions are shown in figure S2c. The loading modulus of the polished pillar was marginally lower than that of the as-fabricated 100nm-diameter pillar. The stress-strain data for both top geometries is characterized by the serrated plastic flow, commonly observed in the deformation of small-scale metals. It is presently unclear why the degree of surface roughness varies with sample size, although we can speculate that the kinetics of the electroplating process changes with the size of the electroplating templates. We observed that the surface roughness became worse with the increasing pillar size across the diameters from 100 to 1000 nm.

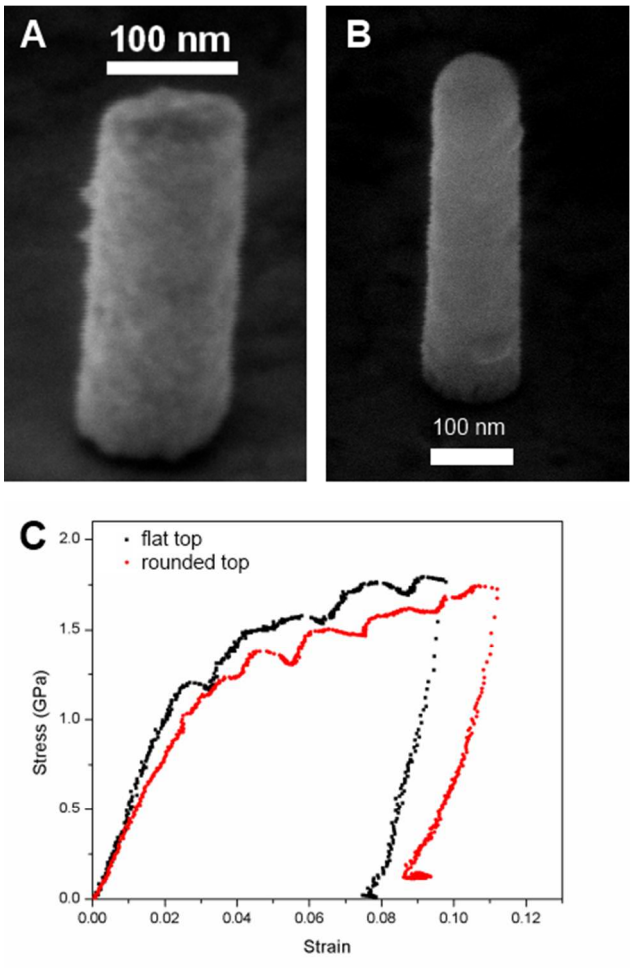

Figure S2. Effect of surface roughness on mechanical behavior of 100 nm sized pillars. SEM images of A) a typical as-electroplated pillar with naturally smooth and flat top and

B) a pillar whose top surface was polished with FIB (hemispherical top). C) Typical stress-strain data for 100 nm sized samples with flat and rounded tops.

The influence of surface roughness is most apparent in the slope of the loading region in the stress-strain curve. The plot in Figure S3 compares the loading slopes between the pillars with smoothed tops vs. as-electroplated ones for a range of pillar sizes. Flattened samples with the diameters between 500 nm and 1 μm consistently had ~40-50% higher loading slopes than their as-fabricated counterparts of equivalent diameters. 100 nm sized pillars were the only samples, for which the loading modulus decreased by ~ 10% as a result of polishing. These trends can be explained in terms of the contact area between the pillar and indenter tip. The presence of surface roughness in a 1 μm-diameter pillar would lead to a reduced contact area and, hence, a lower apparent stress than in a sample with a flat top. FIB-polishing of the smallest, 100nm-diameter samples generated a smaller contact area because of the high degree of curvature, which led to a lower loading slope. There is a negligible difference in the loading modulus of fibbed and as-electroplated 250 nm pillars because of the competing and comparable effects of surface roughness from the electroplating growth process and pillar top curvature induced by the polishing process. The greater degree of strain hardening in the non-flat (i.e. rougher and more curved) pillars can be explained by recognizing that the deformation commenced by the indenter first coming into contact and flattening the raised parts of the pillar surface into the rest of the sample. Once the raised parts of the pillar surface have been compressed, the rest of the test proceeds as compression of a right cylinder.

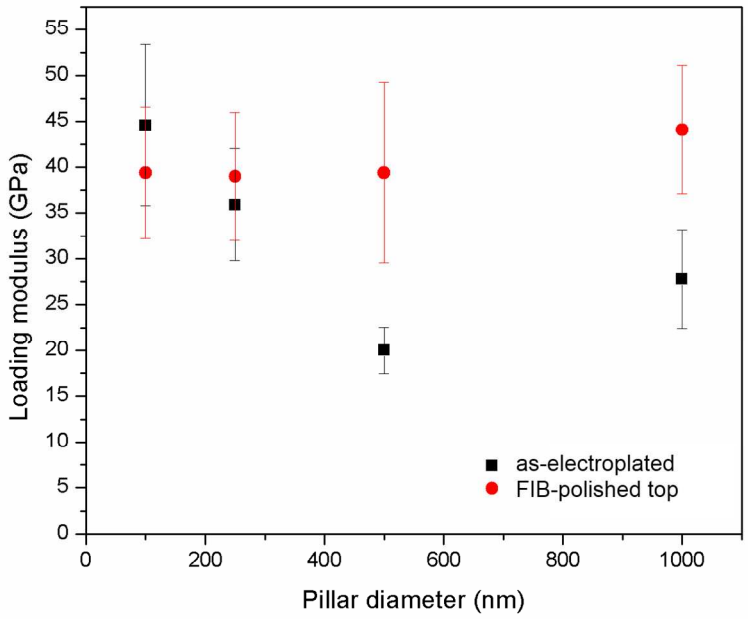

Figure S3. Comparison of loading moduli for pillars with FIB-polished tops and unfibbed (as-electroplated) pillars for a range of pillar diameters from 100 nm to 1 µm.

This analysis shows that the effect of surface roughness cannot be neglected when performing nanomechanical experiments [4,5]. This is especially important for materials with complex microstructures, where the internal microstructural inhomogeneities may be reflected in the surface roughness, whereas single crystalline nanopillars are more likely to have a smooth crystal plane along the surface of the pillar. Care must be taken when interpreting data obtained during these types of experiments.

Detailed examination of grain boundary sliding

Careful examination of grain boundary sliding (GBS) in MD simulations of the nanopillars shows that GBS is of the Rachinger type.

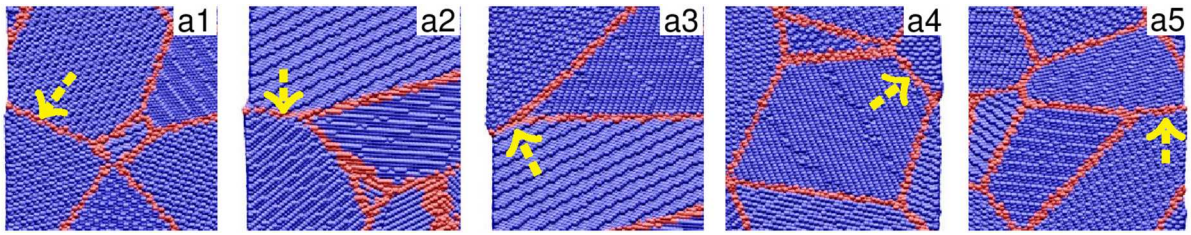

Figure S4. Grain boundary sliding by grains close to the free surface. Yellow arrows point to grain boundaries undergoing sliding. Clearly, grains maintained their original shapes as boundary sliding occurred. The sliding distance at the applied strain is of the order of lattice spacing. The atomistic configurations are taken at 4.3% strain and atoms are colored based on their structural type before the compressive load is applied; blue for atoms at lattice positions and red for atoms at grain boundaries as determined by Common Neighbor Analysis[6]. Note that lattice atoms (blue) would appear in grain boundary regions if diffusion process was actively operating but we do not observe this happening.

Derivation of yield stress formula

The model for yield stress introduced in the main text of the paper can be understood in terms of representing the pillar cross-section as a core-and-shell structure, as schematically shown in Figure S5.

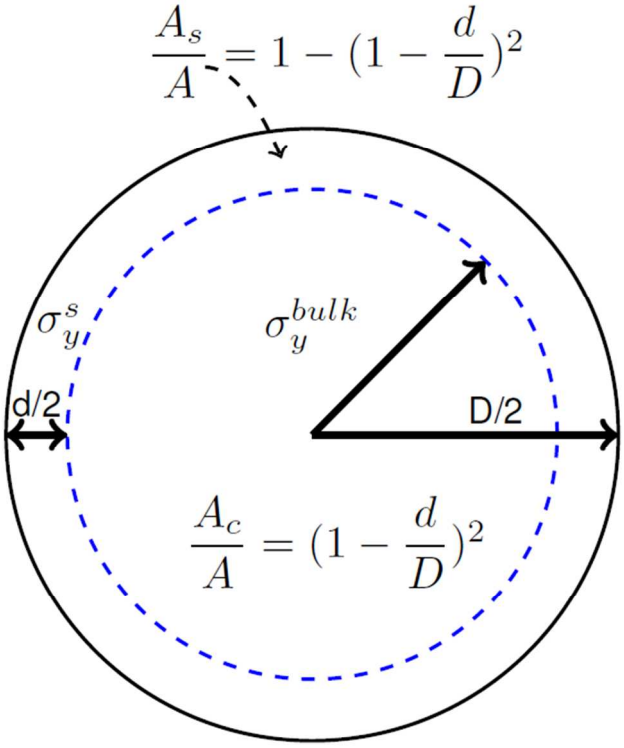

Figure S5. Schematic illustrating model for yield stress showing cross-section of cylindrical sample.

The pillar is divided into a core region with the fractional cross-sectional area $\frac{A_c}{A}$ and an outer shell with the thickness of d/2, whose fractional cross-sectional area is $\frac{A_s}{A}$. It is reasonable to assume that the yield stress of the inner core is equivalent to bulk, σ_y^{bulk}.The yield stress for the outer shell is defined as σ_y^s. Based on geometrical considerations and following the rule of mixtures, these quantities can be related to d and D in the following derivation for yield stress of the nanocrystalline pillar:

$$\sigma_y = \sigma_y^{bulk} \frac{A_c}{A} + \sigma_y^s \frac{A_s}{A} \quad (1)$$

$$\sigma_y = \sigma_y^{bulk} \frac{(D-d)^2}{D^2} + \sigma_y^s \frac{D^2-(D-d)^2}{D^2} \quad (2)$$

$$\sigma_y = \sigma_y^{bulk} \left(1 - \frac{d}{D}\right)^2 + \sigma_y^s \left[1 - \left(1 - \frac{d}{D}\right)^2\right] \quad (3)$$

References

(1) Uchic, M. D.; Dimiduk, D. M.; Florando, J. N.; Nix, W. D. *Science* **2004**, *305*, 986.
(2) Greer, J. R.; Oliver, W. C.; Nix, W. D. *Acta Mater.* **2005**, *53*, 1821.
(3) Zhang, H.; Schuster, B. E.; Wei, Q.; Ramesh, K. T. *Scr. Mater.* **2006**, *54*, 181.
(4) Jahed, Z.; Jin, S. M.; Burek, M. J.; Tsui, T. Y. *Mater. Sci. Eng. A-Struct. Mater. Prop. Microstruct. Process.* **2012**, *542*, 40.
(5) Rinaldi, A.; Peralta, P.; Friesen, C.; Sieradzki, K. *Acta Mater.* **2008**, *56*, 511.
(6) Faken, D.; Jonsson, H. *Computational Materials Science* **1994**, *2*, 279.